# Electronic Supplementary Information

## High-Performance $Sb_2S_3$ Photoanode Enabling Iodide Oxidation Reaction for Unbiased Photoelectrochemical Solar Fuel Production

Young Sun Park, Xiaoyan Jin, Jeiwan Tan, Hyungsoo Lee, Juwon Yun, Sunihl Ma, Gyumin Jang, Taehoon Kim, Sang Gi Shim, Kyungmin Kim, Jeongyoub Lee, Chan Uk Lee, Seong-Ju Hwang*, and Jooho Moon*

*E–mail: hwangsju@yonsei.ac.kr; jmoon@yonsei.ac.kr

**Keywords**: photoanode, antimony trisulfide, iodide oxidation reaction, tandem device, solar hydrogen

**Supplementary Figures**

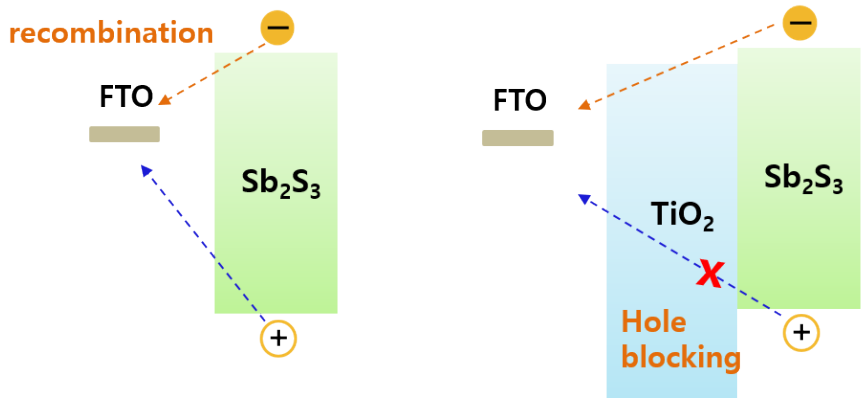


**Fig S1.** Schematics illustrating the role of $TiO_2$ on top of the $Sb_2S_3$ absorber layer as an electron transport layer, while suppressing the recombination of the charge carrier at the back contact.

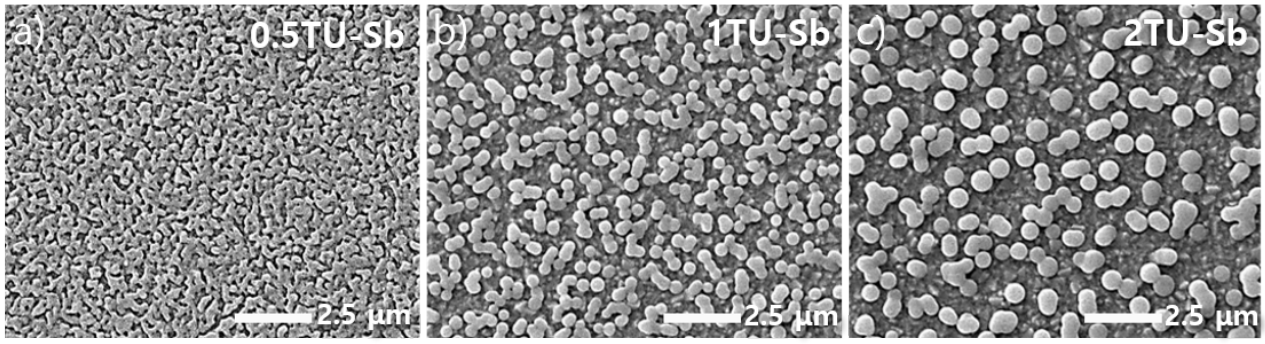


**Fig S2.** Top-view SEM images showing the morphologies of $Sb_2S_3$ films obtained by spin-coating three different precursor inks: a) 0.5TU–Sb, b) 1TU–Sb, and c) 2TU–Sb inks after the solvent drying and annealing processes.

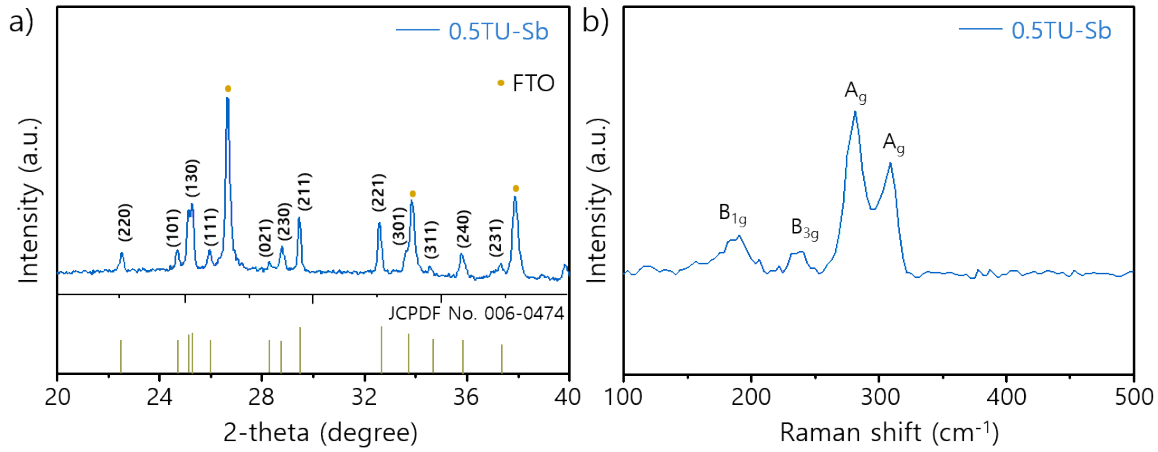


**Fig S3.** a) XRD pattern of the 0.5TU–Sb-ink-based $Sb_2S_3$ absorber. The standard diffraction pattern of $Sb_2S_3$ (JCPDF No. 006-0474) is also shown. b) Raman spectrum of the 0.5TU–Sb-ink-based $Sb_2S_3$ absorber.

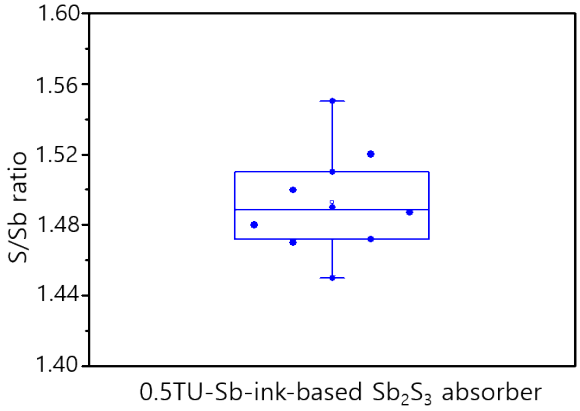


**Fig. S4.** The statistics of SEM-EDX analysis for 0.5TU–Sb-ink-based $Sb_2S_3$ absorber. The middle dots represent the mean value, box edges mean the standard deviations, whiskers indicate the maximum and minimum values in the distributions, while central horizontal line represents the median.

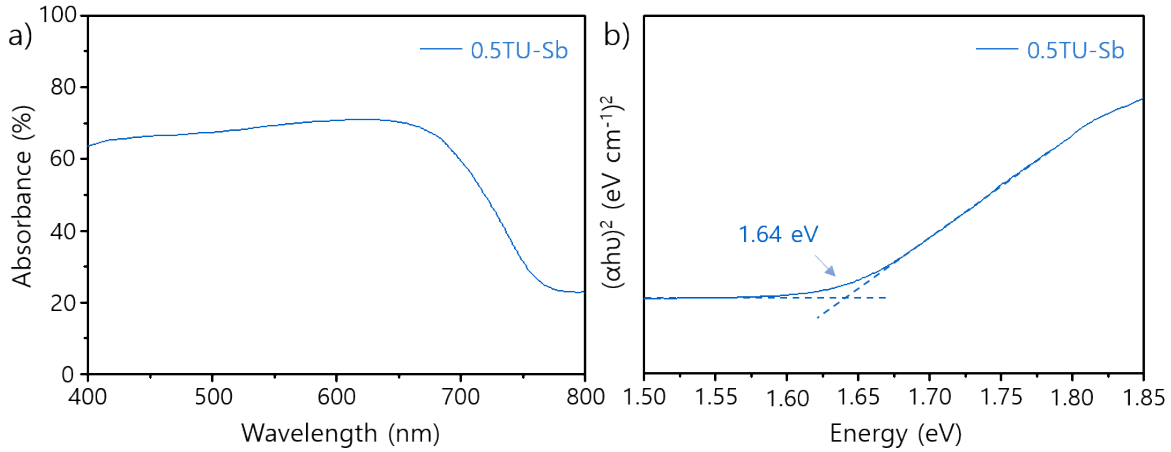


**Fig S5.** a) UV–vis absorbance and b) Tauc plot for the 0.5TU–Sb-ink-based $Sb_2S_3$ absorber.

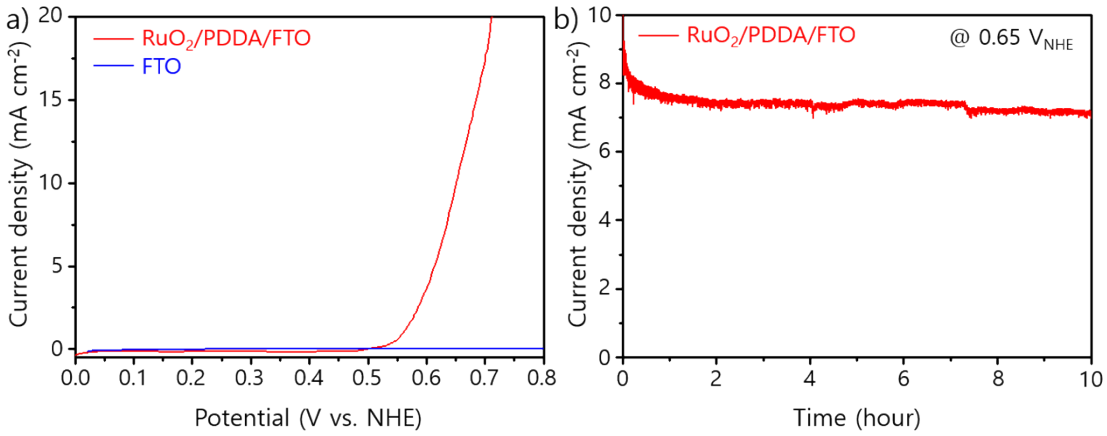


**Fig S6.** a) LSV curves for the $RuO_2$/PDDA/FTO and FTO electrodes in hydroiodic acid (~pH 1). b) Operation stability at 0.65 $V_{NHE}$ for the $RuO_2$/PDDA/FTO electrode in hydroiodic acid.

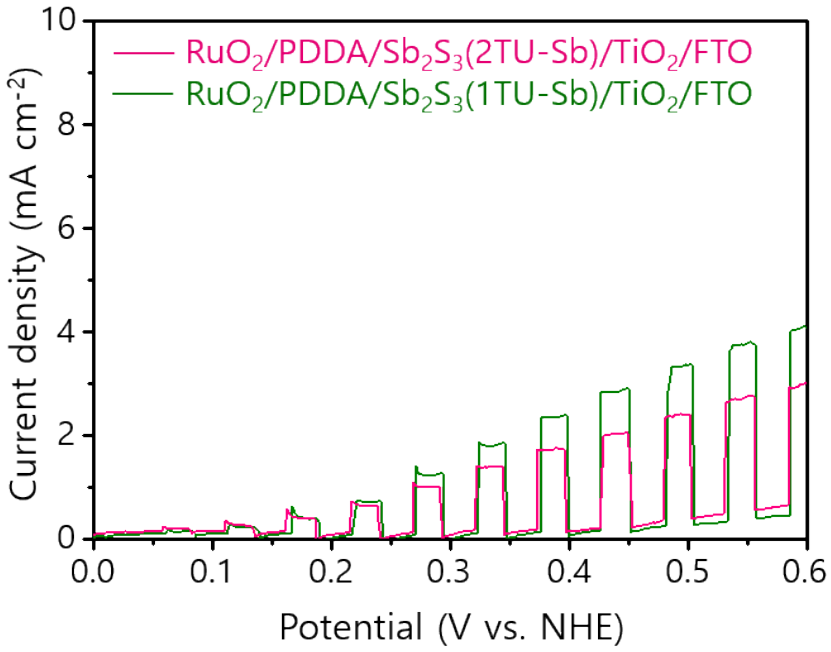


**Fig S7.** LSV curves for the $RuO_2$/PDDA/$Sb_2S_3$(2TU–Sb)/$TiO_2$/FTO and $RuO_2$/PDDA/$Sb_2S_3$(1TU–Sb)/$TiO_2$/FTO photoanodes in hydroiodic acid (~pH 1).

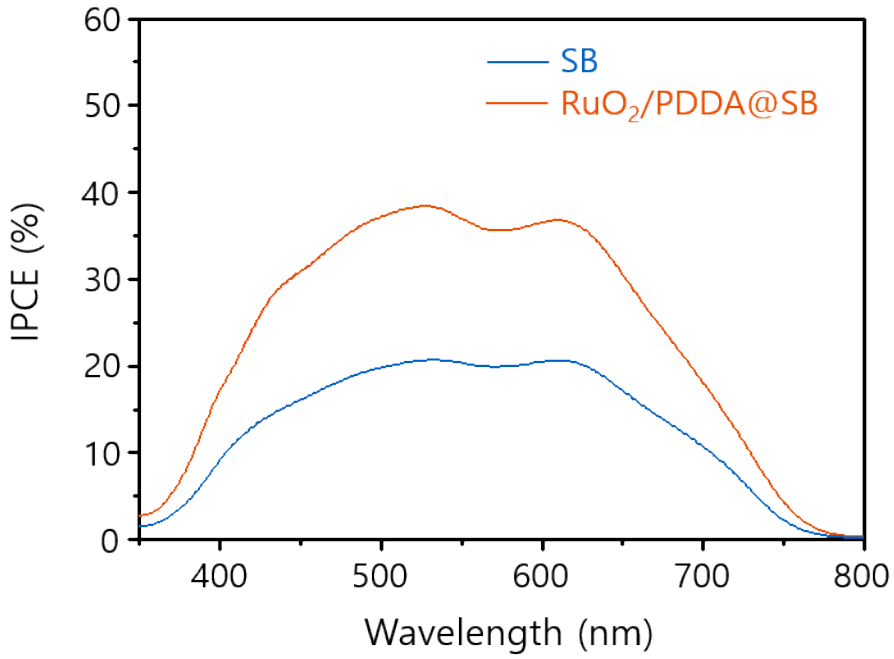


**Fig S8.** IPCE spectra for both SB and $RuO_2$/PDDA@SB photoanodes at 0.35 $V_{NHE}$ in hydroiodic acid (~pH 1).

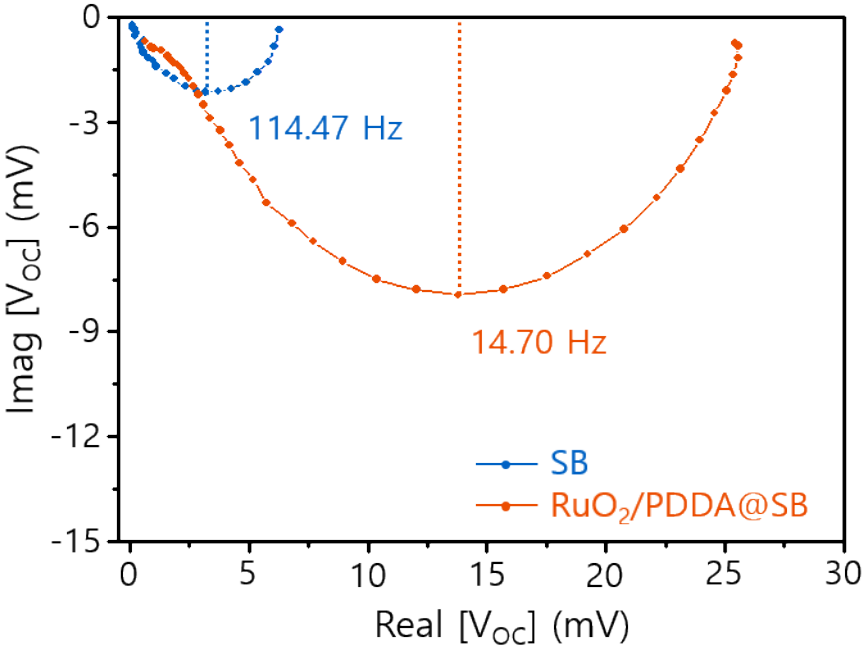


**Fig S9.** Nyquist plots of IMVS spectra for both SB and $RuO_2$/PDDA@SB photoanodes at open circuit potential in hydroiodic acid (~pH 1).

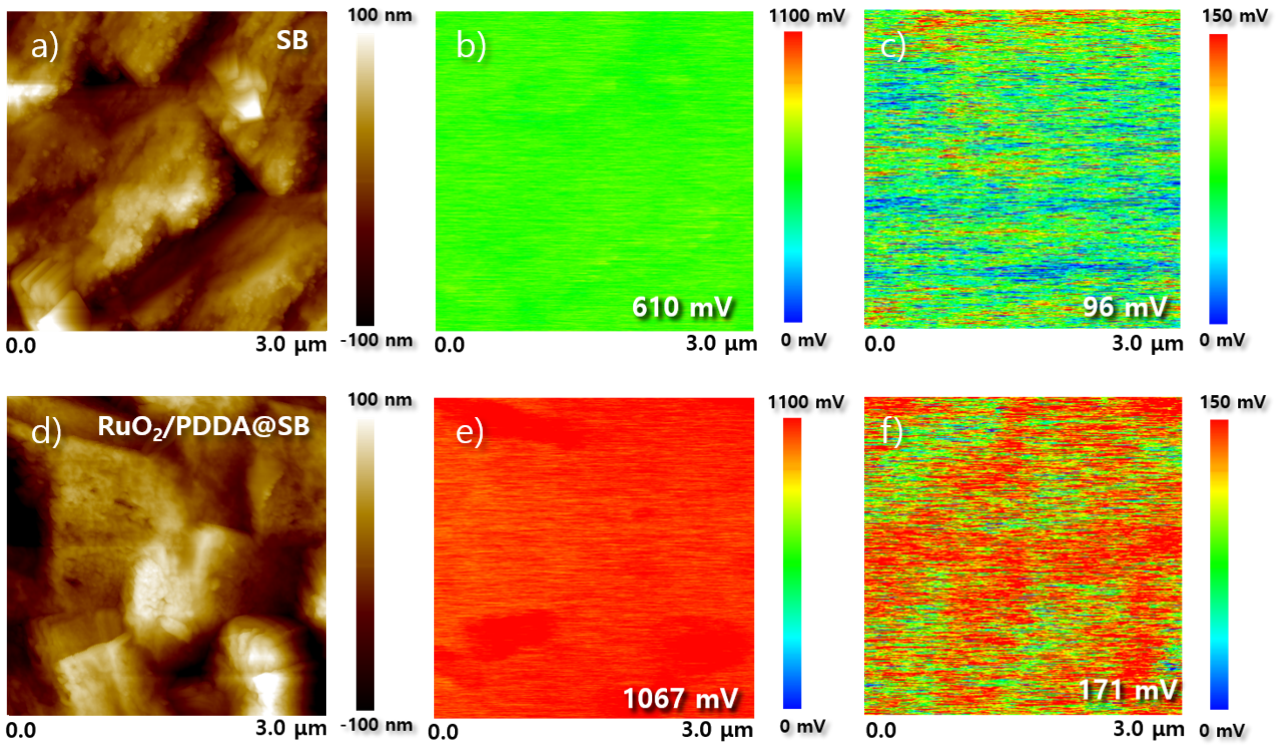


**Fig S10.** Topography image of the a) SB and d) $RuO_2$/PDDA@SB photoanodes. CPD of the b) SB and e) $RuO_2$/PDDA@SB photoanodes. SPV of the c) SB and f) $RuO_2$/PDDA@SB photoanodes.

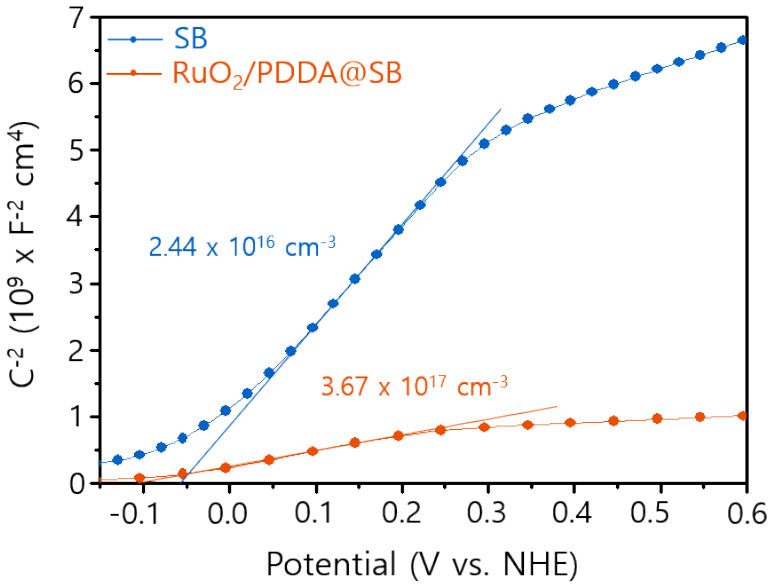


**Fig S11.** Mott-Schottky (MS) plots of the SB and $RuO_2$/PDDA@SB photoanodes in hydroiodic acid (~pH 1). Calculated charge carrier densities of both photoanodes are indicated inside the plot.

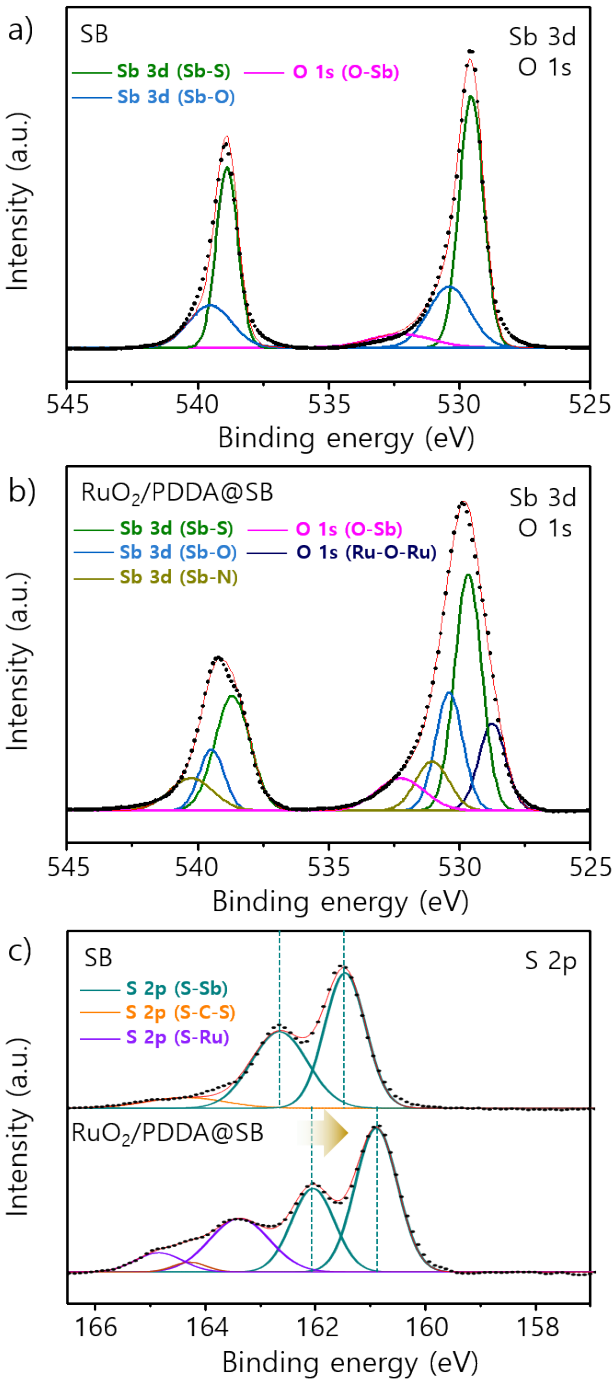


**Fig S12.** a) High-resolution XPS spectra of Sb 3d, O 1s for the a) SB and b) $RuO_2$/PDDA@SB photoanodes. c) High-resolution XPS spectra of S 2p for the two photoanodes.

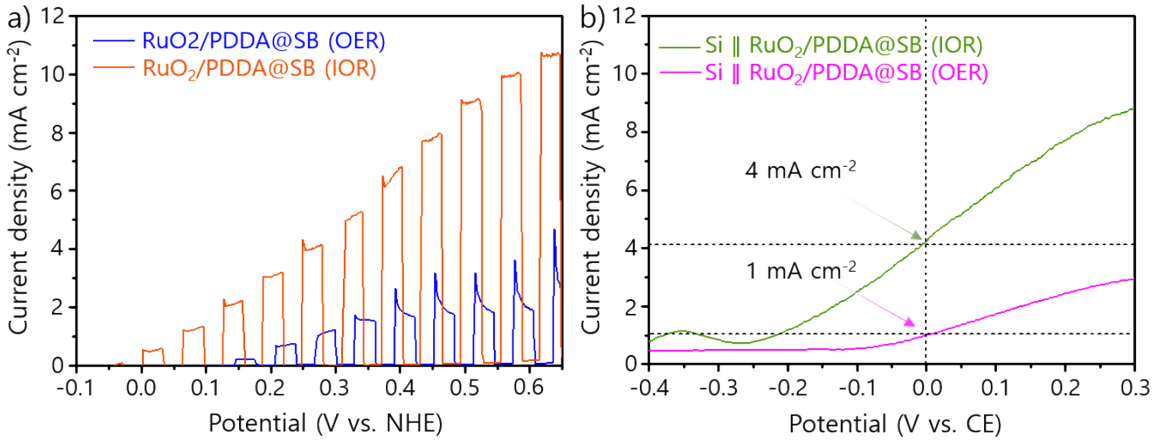


**Fig S13.** a) LSV curves of the $RuO_2$/PDDA@SB photoanode in hydroiodic acid (~pH 1) and sulfuric acid (~pH 1). b) LSV curves of the Si ‖ $RuO_2$/PDDA@SB two-electrode tandem cell (active area: 0.25 $cm^2$) in hydroiodic and sulfuric acids.

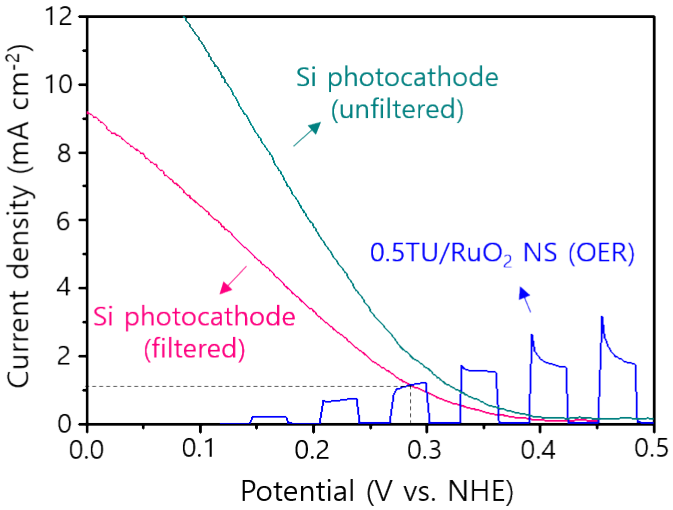


**Fig. S14.** LSV curves of the $RuO_2$/PDDA@SB photoanode and silicon photocathode operated in sulfuric acid.

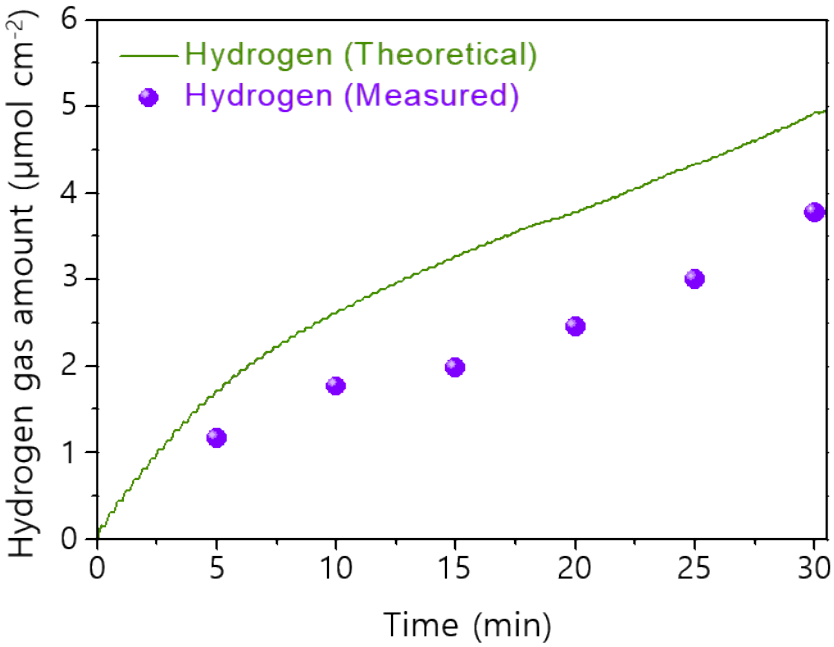


**Fig S15.** Gas chromatography analysis of the Si ‖ $RuO_2$/PDDA@SB tandem cell under short-circuit condition in hydroiodic acid (~pH 1).

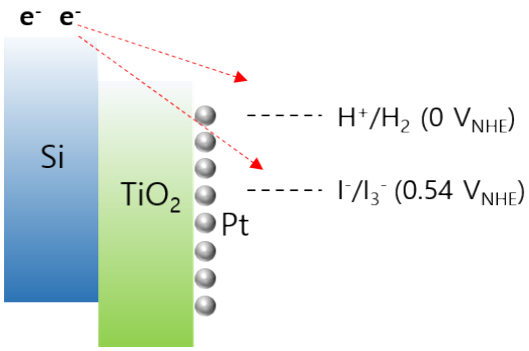


**Fig S16.** Schematic diagram of band structure of silicon photocathodes, HER potential, and iodide/triiodide redox level.

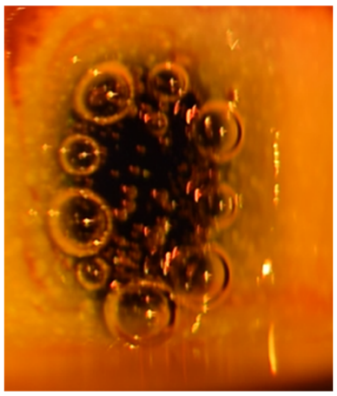

**Fig S17.** Hydrogen edge bubbles that block the surface of silicon photocathode during the PEC operation.

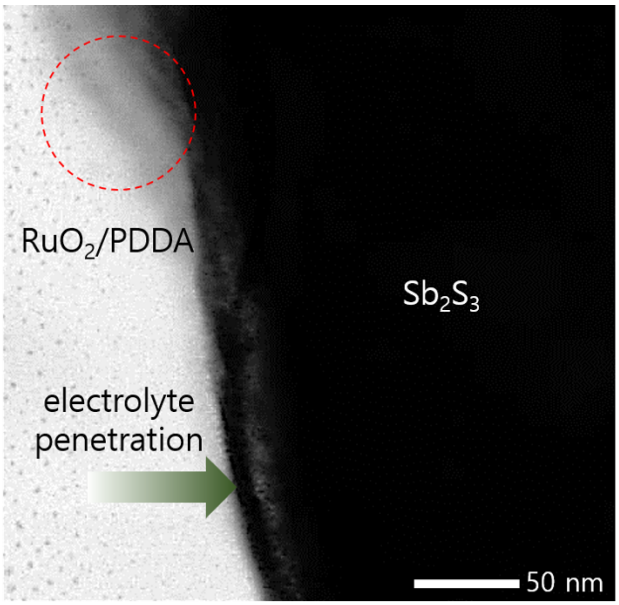


**Fig S18.** STEM image of the $RuO_2$/PDDA@SB photoanode.

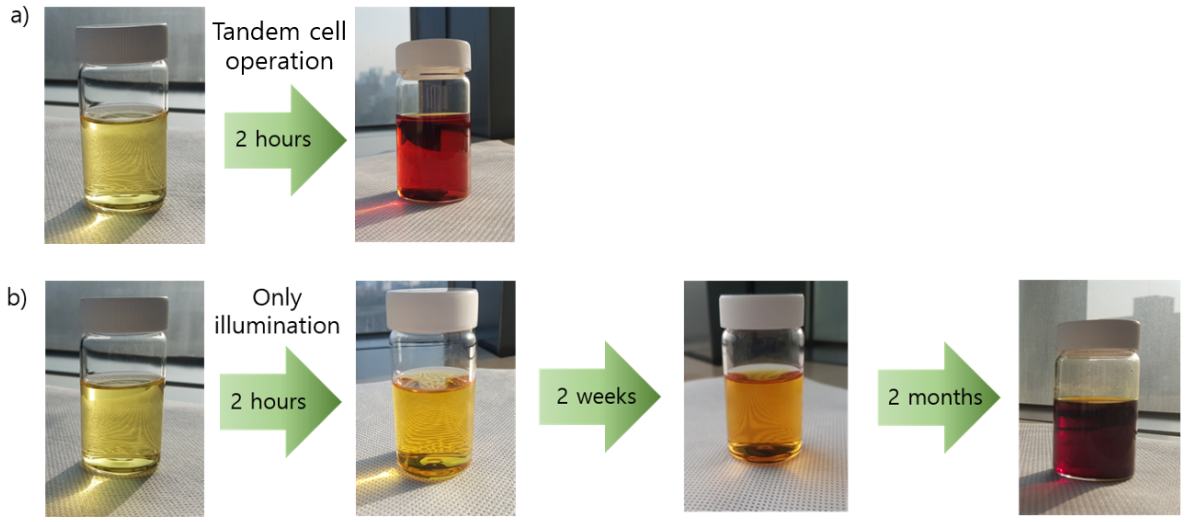


**Fig. S19.** Color change of hydroiodic acid electrolyte a) during the operation of Si ‖ $RuO_2$/PDDA@SB tandem cell and b) spontaneous oxidation reaction expressed as equation ($4H^+ + 6I^- + O_2 \rightarrow 2H_2O + 2I_3^-$, $\Delta G^o < 0$) under illumination without electrochemical reaction.

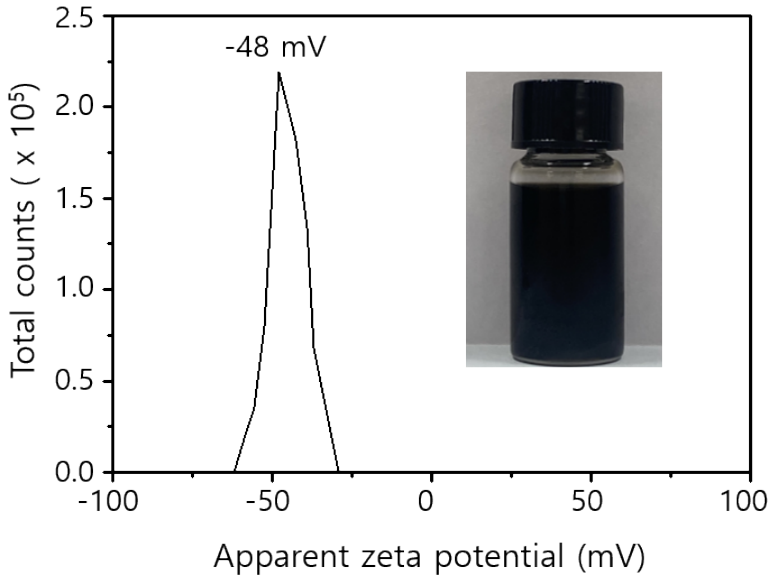


**Fig S20.** Colloidal suspension (inset) and zeta potential data of exfoliated $RuO_2$ NS.

**Supplementary Table S1**. Compositional analysis of the 0.5TU–Sb-ink-based $Sb_2S_3$ absorber via EDX.

| Element | Atomic percent (%) |
|---|---|
| O K | 22.26 |
| S K | 34.63 |
| Sn K | 16.50 |
| Sb K | 23.40 |
| Pt M | 1.07 |
| Ti K | 1.74 |
| Total | 100 |

**Supplementary Table S2.** The composition analysis of $RuO_2$/PDDA@SB determined by TEM-EDX analysis

| Element | Atomic percent (%) |
|---|---|
| Sb | 6.7 |
| S | 10.0 |
| Ru | 0.6 |
| O | 2.5 |
| C | 80.2 |
| Total | 100.0 |

**Supplementary Table S3**. Summarized parameters of EIS for the SB and $RuO_2$/PDDA@SB photoanodes measured at 0.35 $V_{NHE}$.

| Sample | SB | $RuO_2$/PDDA@SB |
|---|---|---|
| $R_S$ ($\Omega \cdot cm^2$) | 1.894 | 3.873 |
| $R_{CT}$ ($\Omega \cdot cm^2$) | 133.3 | 42.94 |

**Supplementary Table S4**. Structural parameters of the SB and $RuO_2$/PDDA@SB photoanodes determined by Sb K-edge EXAFS analysis*.

| Material | Bonding Pair | CN[c)] | R (Å)[d)] | ΔE | $\sigma^2$ (Å$^2 \times 10^{-3}$) [e)] |
|---|---|---|---|---|---|
| SB[a)] | (Sb–S) | 4.0 | 2.59 | 2.80 | 9.96 |
| $RuO_2$/PDDA @SB[b)] | (Sb–S) | 4.7 | 2.60 | 1.63 | 3.36 |

*The curve fitting analysis was performed for the range of [a)]1.626–R–2.700 Å and 3.500–*k*–11.500 Å$^{-1}$; [b)]1.626–R–2.761 Å and 3.450–*k*–11.350 Å$^{-1}$. [c)]Coordination number, [d)]bond distance, and [e)]Debye–Waller factor.

**Supplementary Table S5**. Recent reports on PEC tandem devices for unbiased hydrogen generation.

| Photoanode | Photocathode | Reactions in tandem configuration | Photocurrent density | Ref. |
|---|---|---|---|---|
| Co-Pi/W:$BiVO_4$ | $RuO_2/TiO_2$/AZO/$Cu_2O$ | HER–OER | 1.2 mA $cm^{-2}$ | S1 |
| $NiFeO_x$/Mo:$BiVO_4$ | $RuO_2/TiO_2/Ga_2O_3/Cu_2O$ | HER–OER | 2.4 mA $cm^{-2}$ | S2 |
| $NiFeO_x$/Mo:$BiVO_4$ | Pt/$TiO_2$/CdS/$Sb_2Se_3$ | HER–OER | 1.2 mA $cm^{-2}$ | S3 |
| $NiFeO_x$/CTF-BTh [a] /Mo:$BiVO_4$ | $MoS_x$/CTF-BTh/$Cu_2O$ | HER–OER | 2.95 mA $cm^{-2}$ | S4 |
| $NiFeO_x$-$B_i$/$BiVO_4$ | Pt/$HfO_2$/CdS/$HfO_2$/CZTS | HER–OER | 2.58 mA $cm^{-2}$ | S5 |
| $NiFeO_x$-$B_i$/$BiVO_4$ | Pt/CdS/CIGS | HER–OER | 3.0 mA $cm^{-2}$ | S6 |
| $Co_4O_4$/PGO/$BiVO_4$/$SnO_x$ | Pt/$TiO_x$/PIP[c]/$CuO_x$ | HER–OER | 3.5 mA $cm^{-2}$ | S7 |
| $Bi_2Se_3/TiO_2$/FTO | $CuBi_2O_4$/FTO | HER–SOR[e] | 0.5 mA $cm^{-2}$ | S8 |
| CPN [b]:$SnO_2$/FTO | $RuO_2$/PTB7-Th:PDI-V[d] /$MoO_3$/FTO | HER–IOR | 0.036 [f] mA $cm^{-2}$ | S9 |
| **$RuO_2$/PDDA/$Sb_2S_3$/$TiO_2$/FTO** | **Pt/$TiO_2$/modified p-Si** | **HER–IOR** | **4.0 mA $cm^{-2}$** | **This work** |

[a]covalent triazine frameworks, [b]covalent polymer network, [c]PBDB-T:ITIC:$PC_{71}BM$ [d]donor polymer coded PTB7-Th and acceptor polymer coded PDI-V, [e]sulfite oxidation reaction, and [f] the calculated photocurrent density based on the active area.

**Supplementary Information References**


S1. P. Bornoz, F. F. Abdi, S. D. Tilley, B. Dam, R. van de Krol, M. Graetzel, K. Sivula, *J. Phys. Chem. C,* 2014, **118**, 16959.

S2. L. F. Pan, J. H. Kim, M. T. Mayer, M.-K. Son, A. Ummadisingu, J. S. Lee, A. Hagfeldt, J. S. Luo, M. Gratzel, *Nat. Catal.,* 2018, **1**, 412.

S3. W. Yang, J. H. Kim, O. S. Hutter, L. J. Phillips, J. Tan, J. Park, H. Lee, J. D. Major, J. S. Lee, J. Moon, *Nat. Commun.,* 2020, **11**, 861.

S4. Y. Zhang, H. F. Lv, Z. Zhang, L. Wang, X. J. Wu, H. X. Xu, *Adv. Mater.,* 2021, **33**, 2008264.

S5. D. W. Huang, K. Wang, L. T. Li, K. Feng, N. An, S. Ikeda, Y. B. Kuang, Y. Ng, F. Jiang, *Energy Environ. Sci.,* 2021, **14**, 1480.

S6. H. Kobayashi, N. Sato, M. Orita, Y. Kuang, H. Kaneko, T. Minegishi, T. Yamada, K. Domen, *Energy Environ. Sci*., 2018, **11**, 3003.

S7. S. Ye, W. W. Shi, Y. Liu, D. F. Li, H. Yin, H. B. Chi, Y. L. Luo, N. Ta, F. T. Fan, X. L. Wang, C. Li, *J. Am. Chem. Soc.,* 2021, **143**, 12499.

S8. P. Subramanyam, B. Meena, D. Suryakala, C. Subrahmanyam, *ACS Appl. Nano Mater.,* 2021, **4**, 739.

S9. L. Yao, Y. P. Liu, H.-H. Cho, M. Xia, A. Sekar, B. P. Darwich, R. A. Wells, J.-H. Yum, D. Ren, M. Gratzel, N. Guijarro, K. Sivula, *Energy Environ. Sci.,* 2021, **14**, 3141.